


Borrmann effect in Laue diffraction in one-dimensional photonic crystals under a topological phase transition

V. B. Novikov* and T. V. Murzina

Department of Physics, M. V. Lomonosov Moscow State University, Moscow, 119991, Russia

 (Received 31 January 2019; revised manuscript received 21 May 2019; published 4 June 2019)

We present experimental and theoretical studies of the anomalous high transmission of light (the Borrmann effect) under the Laue diffraction in a one-dimensional photonic crystal (PhC) characterized by spatial modulation of both refractive index and absorption. We show that a strong modulation of the refractive index along with the large PhC period provide new features of the Borrmann effect as compared to the well-known x-ray Borrmann effect in crystals appearing in PhC wavelength-angular transmission spectra. Namely, the maximal transmission is attained at the Bragg angles of incidence and corresponds alternatively to even or odd orders of the Bragg angles depending on the light wavelength. Second, a dramatic decrease of the angular width of the high transmission areas in the spectrum appear near the diabolic points. According to our description, this effect can be treated as a result of the topological phase transition accompanied by exchange of the parity of spatial distribution of the electromagnetic field of the two eigenmodes experiencing degeneracy. We demonstrate that these peculiarities are inherent to the PhC with the optical losses located in layers with higher refractive index, and disappear if the losses are specific for the PhC layers with lower refractive index. The suggested underlying mechanism involves the contribution of the waveguide PhC modes to the PhC transmission spectra.

DOI: [10.1103/PhysRevB.99.245403](https://doi.org/10.1103/PhysRevB.99.245403)

I. INTRODUCTION

The interaction of electromagnetic radiation with periodic systems has been a popular research topic for many decades. The first studies in this field were based on the x-ray diffraction in crystals where the existence of ordered atomic planes led to a number of effects. Among those, one of the most known phenomenon is the Borrmann effect consisting of the suppression of the absorption of the x rays propagating through the crystal at the Bragg angle of incidence in the transmission geometry (the so called Laue geometry) [1–3]. The effect was used in x-ray polarizers [4], monochromators [5], and was considered for applications in gamma-ray laser [6]. It is at Bragg diffraction that there are two strong waves of zero and first diffraction orders, superposition of which forms two electromagnetic modes in the crystal [7]. One of the modes, called the anti-Borrmann one, is localized on atomic planes, suffers strong photoelectric absorption, and decreases faster than the second mode, called the Borrmann one. In turn, the Borrmann mode is localized between the atomic planes of a crystal, so it experiences low absorption and propagates for many attenuation lengths giving anomalous high transmission.

Following the direct analogy between the interaction of the x rays with crystals and of visible light with periodic dielectric systems, the Borrmann effect was revealed at the Laue diffraction of light in holographic gratings formed in a several microns thick photographic emulsion and dyed crystal [8–11]. It was also observed in one-dimensional (1D)

porous silicon based photonic crystals (PhCs) and studied for different mechanisms of losses such as absorption and light scattering [12]. The phenomenon similar to the Borrmann effect was observed at lateral mechanical shifting of light-induced absorption grating in a photochromic material [13]. In the last years, studies of the Laue diffraction in 1D PhCs brought plenty of optical effects such as the pendulum effect, which allows the optical switching based on the coupling of diffraction waves of different orders in PhC [14]; angular asymmetry of the pendulum effect with respect to the angle of incidence in PT-symmetric 1D PhC with the gain and losses [15]; temporal femtosecond pulse splitting [16,17]; and phase- and quasiphase-matched second harmonic generation [18–20]. These phenomena specific for the Laue diffraction are rather perspective for the light manipulation.

The analog of the Borrmann effect appears as well in another diffraction scheme, the so called Bragg one, at the spectral edges of the PhC photonic band gap (PBG). In that case the light localization inside the PhC is different for the short- and long-wavelength PBG edges, forming the nodes of the electromagnetic field inside or between the absorbing layers, so that the anomalous transmission appears in the spectral range that corresponds to one of the PBG edges. Experimentally it was confirmed for circularly polarized light in cholesteric liquid crystals [21] and ones with an admixture of dichroic molecules [22–26]. Besides, the Borrmann effect may appear in higher dimensional PhC structures such as two-dimensional (2D) PhC [27] and metal-infiltrated opals [28,29]. It is worth noting that localization of light in high refractive index layers at the long wavelength PBG edge can be inverted in high-contrast PhC leading to inverse Borrmann-like effect [30]. Anomalous transmission is

*vb.novikov@physics.msu.ru

possible as well in periodic media with modulation of losses and a homogeneous real part of the refractive index, as was revealed in optics [31] and acoustics [32].

The Borrmann effect allows one to minimize the optical absorption at definite wavelengths and thus to amplify optical and nonlinear optical effects. Good examples here are the enhancement of the Faraday effect in 1D magnetophotonic crystals due to the reduction of the absorption in magnetoactive layers [30,33,34], and of self-focusing in 1D nonlinear PhC consisting of alternating linear and nonlinear layers [35].

Optical effects in PhCs are governed by the properties of the band structure. In recent years, the concept of topological invariants initially developed in condensed matter physics was transferred to optics, so that the Chern number, Zak phase and \mathbb{Z}_2 invariant, which classify the pass bands in the bulk of a spatially periodic material, were used for the construction of photonic topological insulators [36]. These structures support the existence of the edge states that are robust against perturbation, lattice disorder, and are backscattering immune [37]. Discontinuous variations of the topological invariants at passing of the system through the band degeneracy make the crossing points of the band structure important for obtaining nontrivial band gaps, creation of the edge, and resonant states at the interfaces of topologically distinct structures. Such states were distinguished in optics [38–42], acoustics [40,43], and mechanics [44].

The possibility of light routing by means of the edge states tolerant to the structure imperfections inspires the studies of the topological phenomena in 2D and three-dimensional (3D) photonic systems. Since the discovery of the optical analog of the quantum Hall effect [45] exploiting breaking of the time-reversal symmetry in gyromagnetic material subjected to a magnetic field, different approaches were developed to eliminate the usage of weak magneto-optical effects for the robust light transport. In particular, an asymmetric hopping phase in a 2D array of coupled ring cavities was used for generating a synthetic magnetic field that led to topologically nontrivial PBGs [46,47]. The inversion symmetry breaking in gyroid 3D PhCs [48] or 3D helical waveguide arrays [49] leads to the appearance of nontrivial band structure associated with the paired Weyl points, which is a 3D linear point degeneracy between the two bands [43,48,50]. In this case, topologically protected 2D chiral surface modes are guaranteed by the Fermi arc connecting these degeneracy points with the opposite chirality.

Photonic structures of lower dimensions, such as 1D PhCs, can demonstrate topologically protected edge states as well by tuning the surface impedance. Topological properties of the photonic bands of 1D PhCs with inversion symmetry are described by the Zak phase, which is a 1D analog of the Berry phase [51] accumulated by an eigenstate at its movement across the Brillouin zone. The Zak phase is related to the surface impedance [39] and can be determined from the reflection phases in the band gaps [52]. The band gap closing and reopening change the surface impedance and switch the Zak phase, allowing one to realize a resonant edge state at the interface of two topologically distinct 1D PhCs [40,41,53]. This approach was used to predict the edge states in hybrid plasmonic-photonic systems consisting of graphene layers [42], as well as giant enhancement of the third

harmonic generation in a plasmonic film placed between two PhCs [54] and laser generation in a PhC nanocavity [55].

In the absence of the inversion symmetry of the 1D PhC an additional concept for the realization of the edge states at the PhCs/substrate interface was proposed, which is based on the synthetic Weyl points in the 3D parameter space (the Bloch wave number and two unit cell parameters) instead of momentum space [56,57]. The existence of the interface states is guaranteed by the vortex structure of reflected light phase around a synthetic Weyl point.

As opposed to solid state physics, photonic systems have intrinsic losses related to light scattering, leakage, absorption, or gain. Non-Hermiticity gives one the possibility to study the topological transition employing the bulk dynamics instead of probing the surface states. This approach was used to demonstrate the winding number of a 1D topological waveguide system [58]. Non-Hermiticity leads also to the appearance of the exceptional points (EPs) or branch points that are another type of the band degeneracies [59]. The EPs are accompanied by a number of unusual topological phenomena such as mode switching at encircling EP [60,61], generation of the half-integer vector-vortex beams [62], the exceptional ring in 2D PhC [63], and the bulk Fermi arc connecting paired EPs in 2D PhC, which originates from non-Hermiticity rather than the Weyl points in 3D PhC [62].

In the context of the topological photonics, the parity-time (PT) symmetric structures are of particular interest as a special class of non-Hermitian photonic systems combining gain and loss, and resulting in real eigenvalue spectra despite their non-Hermiticity. In 1D PT -symmetric PhCs the angular asymmetric pendulum effect and asymmetric wave enhancement [15,64], and unidirectional pulse splitting effect [65], were predicted at the Laue diffraction, while the unidirectional reflection and asymmetric transmission phase [66] were revealed at the Bragg diffraction scheme.

In this work we study the Borrmann effect at the Laue diffraction in absorptive 1D PhC under the topological phase transition. The PhC is designed to demonstrate multiple crossing points in the band structure due to the inversion symmetry, sufficiently high refractive index contrast, and large PhC period. In the crossing points the band inversion takes place, which is described as the topological transition associated with a discontinuous jump of the Zak phase and the symmetry change of the eigenmodes. We demonstrate that it leads to several pronounced peculiarities of the Borrmann effect in photonic structures in contrast to that in the x rays. We show that incorporation of slight optical losses to the PhC making it a non-Hermitian system allows us to visualize the topological transitions using the bulk properties of the PhC instead of the interface states, which were used in previous works on the topological properties of 1D PhCs. As well we revealed crucial difference of the light transmission through the PhCs as the losses are specific to the layers with high or low refractive indices. Our work complements the studies of the topological properties of 1D PhC performed mostly in the Bragg diffraction geometry. To the best of our knowledge, the topological properties of light transport in 1D PhCs at the Laue diffraction scheme were not studied thoroughly especially in the aspect of lossy PhCs and the Borrmann effect.

The rest part of the paper is organized as following: Sec. II describes the procedure of the samples' fabrication and the experimental results, Sec. III presents the theoretical description of the observed peculiarities and prediction of the qualitative changing of transmission at switching of absorbing layers to low refractive index ones, followed by the conclusions.

II. EXPERIMENTAL DETAILS

The studies were carried out for the 1D PhC with the two-layered elementary cell fabricated by electrochemical etching of silicon described in detail elsewhere [67]. In brief, a p^{++} boron-doped silicon wafer with (001) orientation and resistance of $\rho = 0.005 \Omega \text{ cm}$ served as the anode in the two-electrode electrochemical cell, the cathode was a flat tungsten spiral, and 28% hydrofluoric acid solution was used as an electrolyte. Electric current application through the cell led to the random growth of the pores inside the Si wafer oriented along the [001] crystallographic axis (perpendicular to the wafer-liquid interface). Using the dependence of the porosity of silicon on the current density j , the meanderlike periodical temporal j modulation with the values $j_1 = 16 \text{ mA/cm}^2$ and $j_2 = 170 \text{ mA/cm}^2$ gave the layered structure. Then the current with the high density of 1 A/cm^2 was applied in order to get the free-standing PhC, which was later dried at ambient conditions. The obtained PhC consisted of 240 alternating layers with equal thicknesses of $d_1 = d_2 = 1450 \text{ nm}$, their porosities being $p_1 = 0.57$, $p_2 = 0.73$, and the pore diameters of $\delta_1 = 19 \pm 8 \text{ nm}$, $\delta_2 = 65 \pm 28 \text{ nm}$ as measured by a low-temperature nitrogen adsorption technique. Since pore sizes are considerably smaller than the light wavelength, optical properties of the silicon-air composite layers of the PhC were described by the effective refractive indices $n_1(800 \text{ nm}) = 2.00 + i2.2 \times 10^{-3}$, $n_2(800 \text{ nm}) = 1.50 + i0.8 \times 10^{-3}$.

At the next stage, thermal annealing of the PhC was performed at the temperature of 750°C for 30 min. These parameters were chosen to provide the full annealing of the high porosity layers to porous silica, while low porosity layers were partially annealed and consisted of silica, silicon, and air. The spatial periodicity of silicon distribution in the PhC was confirmed by luminescence microscopy [12]. The annealing increased the optical transparency of the PhC making it convenient for carrying out transmission optical experiments, and increased as well the depth of the absorption coefficient modulation making the light penetration through the periodic structure more sensitive to the light localization inside the PhC. Finally, the refractive indices of the PhC were $n_1(800 \text{ nm}) = 1.76 + i1.6 \times 10^{-3}$, $n_2(800 \text{ nm}) = 1.11 + i2 \times 10^{-5}$, the layers' thicknesses $d_1 = d_2 = 1450 \text{ nm}$, the period was $d = d_1 + d_2 = 2900 \text{ nm}$, and the geometrical sizes: length $L = 500 \mu\text{m}$, width $w = 350 \mu\text{m}$, height 5 mm (Fig. 1).

It is necessary to note that light losses take place in low porosity absorptive layers, while high porosity layers are transparent and have negligibly small losses associated with the light scattering in pores. Interfaces between the layers of different porosity are well defined; SEM images of the PhC' edge show that the roughness of these interfaces is about 40 nm , which is much smaller than the wavelength of light used in experiments.

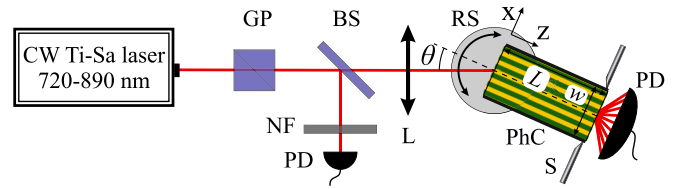


FIG. 1. Scheme of the experimental setup. The used elements: GP: Glan prism, BS: beam splitter, NF: neutral filter, PD: photodiodes, RS: rotation stage, S: slit.

The scheme of the experimental setup is shown in Fig. 1. The s -polarized beam of a continuous wave titanium-sapphire laser tunable in the wavelength range of $\lambda = 720\text{--}890 \text{ nm}$ was focused on the sample to a spot of about $90 \mu\text{m}$ in diameter by a lens with the focal distance of $f = 25 \text{ cm}$. It gave the confocal parameter of the focused beam of 14 mm that is considerably smaller than the PhC length L . The sample was mounted on the rotation stage. The photodiode with large sensitive area of 78.5 mm^2 placed close to the end facet of the PhC gathered the radiation passed through the PhC including all diffraction maxima.

Figure 2 shows the angular dependencies of the PhC total transmission for different light wavelengths λ on the tangential component of the incident wave vector $k_x = k_0 \sin(\theta)$, where θ is the angle of incidence and $k_0 = 2\pi/\lambda$ is the vacuum wave number. In Fig. 2(a) each of the horizontal cross sections of the transmission is normalized to its own maximum for better visibility of the data, which avoids the spectral dependence of the light absorption of silicon that influences the registered transmission. Figure 2(b) shows the cross sections of the data plotted in Fig. 2(a) for the wavelengths of 770 and 812 nm without normalization. One can see a set of maxima that corresponds to the Bragg angles θ_m of different orders m defined as $2d \sin(\theta_m) = m\lambda$, $m \in \mathbb{Z}$, which correspond to $k_x = mh/2$, $h = 2\pi/d$ being the length of the PhC reciprocal lattice vector, manifesting the optical

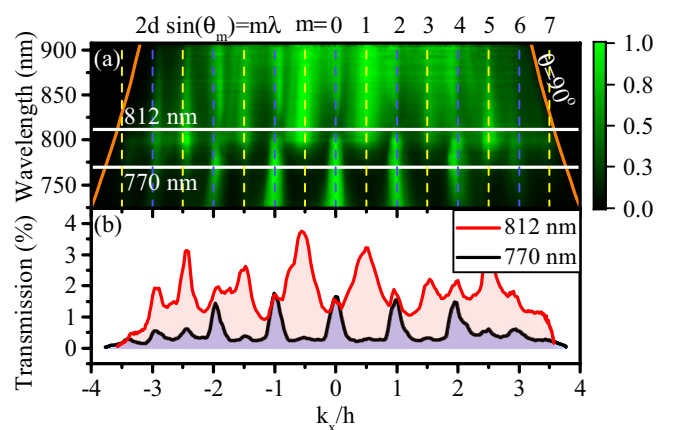


FIG. 2. (a) Spectral-angular dependence of the normalized transmission of the PhC; $k_x = (2\pi/\lambda) \sin(\theta)$ is the tangential component of the incident wave vector, θ is the angle of incidence, λ is the wavelength of light, $h = 2\pi/d$ is the reciprocal lattice vector, and d is the PhC period. Solid orange lines correspond to the light cone, vertical dashed lines to $k_x = h/2m$, where m is the order of the Bragg angle. (b) Cross sections of (a) for 770 and 812 nm wavelengths.

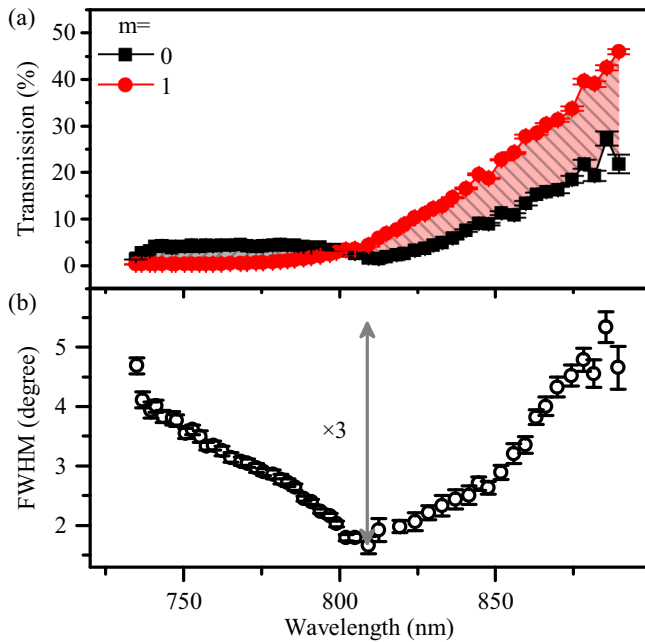


FIG. 3. Spectral dependencies of (a) the amplitudes of the maxima $m = 0$ and $m = 1$, and (b) FWHM of the central transmission maximum near $\theta = 0^\circ$.

Borrmann effect. Importantly that the large lens focal distance (25 cm) in our experiments was chosen in order to provide the spatial spectrum of the focused beam ($\sigma_b \approx 0.4^\circ$) to be narrower than the typical width of the transmission maxima ($\sigma_m \approx 3.5^\circ$). This, more than 8 times difference of the widths σ_b and σ_m , gives high enough visibility of the angular transmission maxima.

It stems from Fig. 2 that depending on the light wavelength the transmission maxima correspond to the Bragg angles of odd or even orders m . To reveal this clearly, each cross section is fitted by a superposition of the required number of Gaussian curves. The obtained spectral dependence of the amplitudes of the two maxima $m = 0$ and $m = 1$ is shown in Fig. 3(a). The amplitude of the central maximum ($m = 0$) dominates for short wavelengths ($\lambda < 800$ nm), while the amplitude for $m = 1$ dominates for long wavelengths ($\lambda > 800$ nm), manifesting the swap of high transmission between odd and even Bragg order maxima at wavelength changing. This exchange is affected by the decrease of the absorption of Si nanograins with increasing wavelength, which leads to fast growth of the transmission amplitudes as shown in Fig. 3(a). Moreover, in the case of domination of the maxima of even orders, the anomalous transmission appears at normal incidence as well. We note that for the x rays in crystals the anomalous transmission is absent for the normal incidence since the Bragg diffraction does not occur and nonuniform field distribution in the crystal is not formed. The observed feature appears due to high refractive index contrast of the PhC, which turns out to be enough for the formation of nonuniform field distribution even at normal incidence as described below.

Another peculiar effect to be discussed is the spectral dependence of the angular width of even-order transmission maxima on the light wavelength, which demonstrates the minimum at 808 nm [Fig. 3(b)]. The observed narrowing is

at least 3 times, as can be seen in Fig. 3(b). It is worth noting that the waist of the beam at this wavelength is smeared by the finite divergence of the incidence beam σ_b and possibly by irregularities of PhC's input edge surface that arose at PhC cleaving. It can be reduced further by the surface flattening and if a focusing lens with longer focus is used.

To the best of our knowledge, the revealed features of the light transmission through the PhC have not been described previously and demonstrate peculiarities if compared to known results of the x ray and the optical Borrmann effects. As is shown in the theoretical part below, these features can appear only for the PhC with high refractive index contrast and large PhC period as compared to the probe wavelength, thus they are peculiar to photonics rather than to the x rays.

III. THEORETICAL DESCRIPTION

The calculation of the light diffraction in the PhC was carried out by means of the rigorous coupled-wave analysis (RCWA) [68], which is based on the Fourier expansion of the electromagnetic fields and of the dielectric function of the PhC. The simulation was carried out for the PhC with the same parameters as in the experiment (see Sec. II) and when neglecting the dispersion of the complex refractive indexes of all the constituent materials. In this approximation the spectra are more clear, while their main features remain qualitatively the same. Figure 4(a) shows the calculated spectral-angular total transmission of the PhC, the shaded area indicates the spectral region studied in the experiment. The spectrum demonstrates a set of high transmission angular maxima centered at $k_x = mh/2$, which correspond to anomalous transmission not only at the Bragg angles but at normal incidence as well, which agrees with the experimental observations. Moreover, the calculated spectrum reveals alternation of the maxima at the Bragg angles of even and odd orders when the wavelength is changing. So the maxima are staggered in the spectral-angular space as in the experiment [Fig. 2(a)]. We note that there is a difference between the experimental and numerical results, namely the appearance of odd order maxima in the experimental spectrum at smaller wavelength as compared to the numerical one. This difference stems from the dispersion of absorption of Si inclusions that are present in the PhC as was mentioned above. Each maximum is a bowtielike and has the waist at the wavelength denoted hereafter as λ^* , where the angular width of the maximum is the smallest and transmission changes abruptly with small angular variations close to the corresponding Bragg angle, which confirms experimentally observed narrowing of the maxima [Fig. 3(b)]. In Fig. 4(a) these wavelengths are indicated by $\lambda_{m,1}^*$. Note that the nodal points along the horizontal line correspond to the same wavelength λ^* . Additionally we emphasize that transmission in nodal points remains high and only the angular width of the transmission maximum is minimal.

The mechanism underlying the appearance of bright spots in the PhC transmission spectra, which correspond to the Borrmann effect, is related to diffraction-induced nonuniform field distribution in the PhC. For the description of this effect, we analyzed the eigenmodes of light in the PhC. In what follows we consider the central maximum in the shaded area

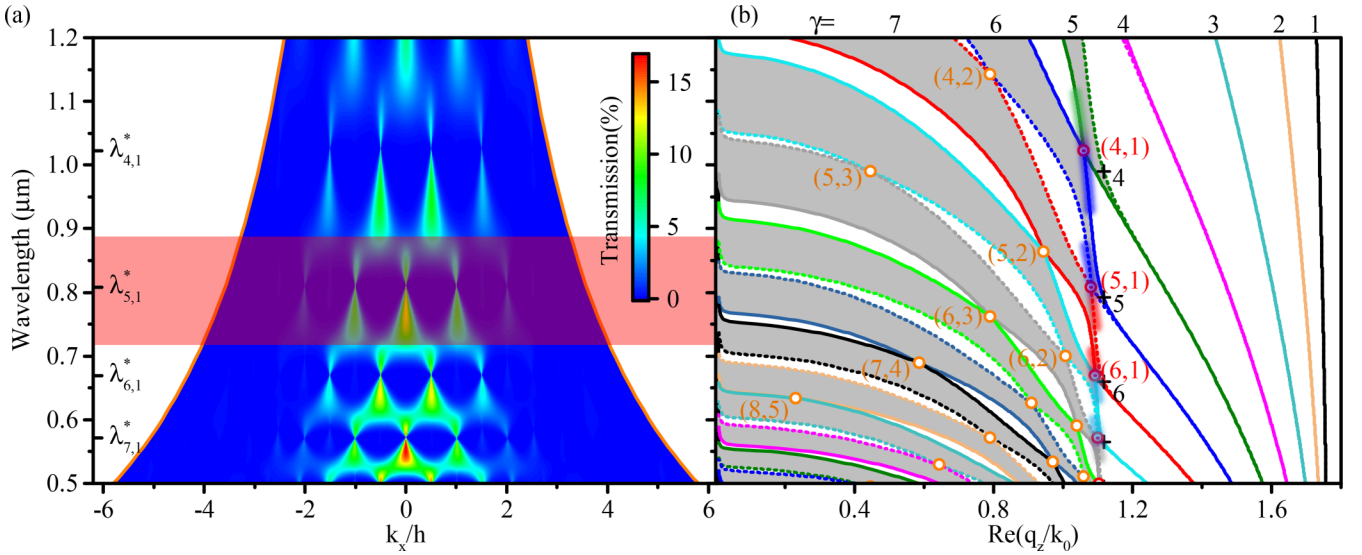


FIG. 4. (a) Calculated spectral-angular dependence of the total transmission of the PhC. The shaded region corresponds to the Ti-Sa laser tuning range. Solid orange lines correspond to the light cone. $\lambda_{m,1}^*$ is the wavelength of diabolic point $(m_1, 1)$ defined by Eq. (3). (b) Projected band diagram of the PhC. The index γ indicates the serial number of dispersion sheet. Dashed and solid lines are the spectral dependencies of the normalized propagation constants $\text{Re}(q_z/k_0)$ of the modes in the center and edges of the Brillouin zone of the PhC, respectively. The crossing points (circles) are labeled by pair of integer numbers (m_1, m_2) according to Eq. (3). The “+” symbol indicates the transition to the waveguide propagation at $\lambda_{m_1}^{\text{wg}}$ where the integer m_1 is near the symbol “+”. The highlighted regions indicate the parts of dispersion curves, which give the transmission maxima.

shown in Fig. 4(a) that fetches out the experimentally accessible spectral region; the analysis remains valid for other spectral maxima as well. Each TE-polarized mode with the electric field parallel to the y axis is the Bloch mode $E_\gamma(x, z) = A_\gamma(x) \exp(iq_z^{(\gamma)} z) \exp(ik_x x)$ characterized by the propagation and attenuation constants $[\text{Re}(q_z^{(\gamma)}), \text{Im}(q_z^{(\gamma)})]$, the amplitude spatial distribution $A_\gamma(x)$, and number γ of the Bloch mode.

To describe the observed angular narrowing and wavelength boundedness of the maxima, we analyze the dependencies of the mode losses and field distribution on k_x for the wavelength λ^* that corresponds to the nodal point of the central maximum in the shaded region in Fig. 4(a) and on the wavelength at $k_x = 0$, i.e., in horizontal and vertical cross sections of Fig. 4(a) passing through the nodal point of the central maximum. The isofrequency curves of light in the PhC, which are the dependencies of the real and imaginary parts of $q_z^{(\gamma)}$ on the tangential component of the wave vector k_x , are shown in Figs. 5(a) and 5(b) at $\lambda = 808 \text{ nm} \gtrsim \lambda^*$, which corresponds to almost the closed gap between the sixth and seventh isofrequency curves. At the crossing point, the gap is closing and the modes have the same phase velocities.

High values of the refractive index, as well as of the PhC period compared to the considered light wavelengths, result in the appearance of a large number of modes that equals 11 for the considered PhC. At the same time, the transmission through the PhC is specified by very few of them. This is illustrated by Figs. 5(a) and 5(b) showing the dispersion of the real and imaginary parts of $q_z^{(\gamma)}$. Indeed the first five modes with $\gamma = 1-5$ reveal flat isofrequency curves that correspond to the waveguidelike propagation of

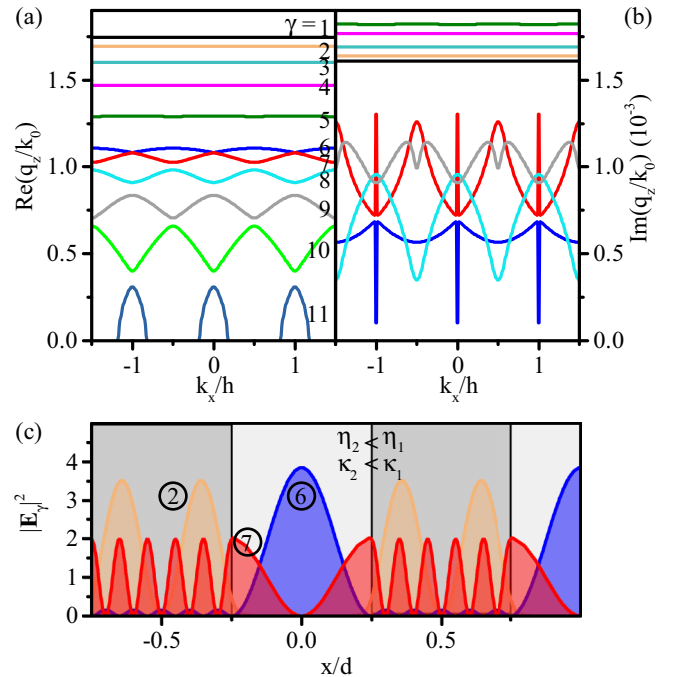


FIG. 5. Propagation (a) and attenuation (b) constants of the eigenmodes with the mode number $\gamma = 1-11$ of the PhC as a function of the tangential component of the wave vector k_x for the light wavelength $\lambda = 808 \text{ nm} \approx \lambda^*$. (c) Spatial distribution of squared electric field of the modes $\gamma = 2, 6, 7$ at $k_x/h = 0, \pm 1, \dots$. The numbers in the circle near the curves denote the mode index γ . Refractive index of layers $n_j = \eta_j + i\kappa_j$. High- and low-absorptive layers are shown by dark and light gray, respectively.

light in PhC. For example, the orange curve in Fig. 5(c) shows the localization of the waveguide modes with $\gamma = 2$ in the high refractive index layers, where the absorption is introduced by Si nanocrystals present in partially annealed layers. So the waveguide modes have a high attenuation constant comparable to the one of the bulk material with the refractive index n_1 , and is about 1.6×10^{-3} [Fig. 5(b)]. Higher order modes have high attenuation constants as well.

We assert that for a particular λ^* wavelength the smallest attenuation in the PhC is realized at crossing of the two modes with $\text{Re}(q_z/k_0) \lesssim n_2$ [Fig. 5(b)]. It is near this propagation constant one of the crossing modes is localized in low absorption layers with the refractive index n_2 . In the considered case, the mode with $\gamma = 6$ possesses the single antinode in low refractive index layers and a small field amplitude in absorbing layers [Fig. 5(c)]. Consequently, this mode has very small absorption, which is 16 times smaller absorption as compared to that in bulk material with n_1 [Fig. 5(b)]. So the light transmission through the PhC for the critical wavelength λ^* is high chiefly due to the presence of the sixth mode, which has the smallest losses, while other modes decay rapidly and do not reach the output PhC facet.

The angular width of the attenuation constant dip of the sixth mode defines the width of the transmission maxima. It is minimal for the gap closing at the wavelength λ^* and leads to the appearance of the nodal points in the spectral-angular dependence of the transmission. Rapid angular changing of $\text{Im}(q_z)$ in vicinity of the crossing point is attributed to variation of the electromagnetic field of the mode at k_x deviation from $0, \pm h/2, \dots$, at which strongly localized modes transform to weakly localized ones having comparable field amplitudes in absorbing and nonabsorbing layers. This field transformation will be demonstrated further when discussing the topological phase transition in the PhC.

So high sensitivity of the light absorption and localization is related to the linear dispersion near the crossing point, where the dispersion surfaces are the double cone (diabolo) with the apex at the degeneracy frequency, so that the crossing point is known also as the diabolic one [Fig. 6(a)]. Linear dispersion in the diabolic point can be confirmed directly from the Taylor series of Eq. (1). In that case, the angular region (k_x range) of the Bragg diffraction associated with bending of the dispersion surface near the center or edge of the Brillouin zone goes to zero and therefore leads to a narrow Bragg diffraction region and thus to the appearance of a nodal point in the transmission spectrum.

More accurately, the band degeneracy in a PhC made of lossy materials is achieved along the arc in (k_x, q_z) plane instead of the point. Its known effect resulted from the non-Hermite perturbation [59] and was exploited in 2D PhCs [62,63]. Nevertheless, when taking into account that the absorption in the considered PhC is rather low, in what follows we will consider the pointlike band degeneracy.

We obtain the position of the crossing points by considering the explicit expression of light dispersion in a 1D

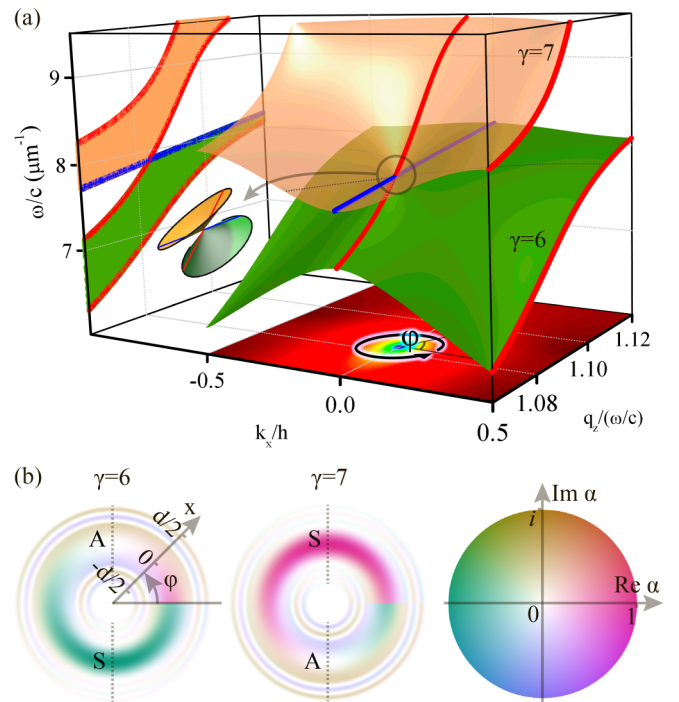


FIG. 6. (a) Dispersion surfaces $\gamma = 6, 7$ and projected band diagram for s -polarized light in the PhC. The red (blue) line indicate even (odd) eigenstates. The color map is the difference of frequencies of the two surfaces. The inset illustrates touching of the conical dispersion sheets at the diabolic point. (b) The distribution of complex electric field of modes $\gamma = 6, 7$ along the circular path shown by an arrow in (a). The radial direction corresponds to x -coordinate, angle φ to point at the circle. The right picture is the color map for the complex number plane; color is phase, color saturation is the absolute value of the complex number.

PhC [69]:

$$\begin{aligned} \cos(k_x d) &= \cos(k_{1x} d_1) \cos(k_{2x} d_2) \\ &\quad - \mathcal{A} \sin(k_{1x} d_1) \sin(k_{2x} d_2), \\ k_{ix} &= \sqrt{\left(n_i \frac{\omega}{c}\right)^2 - q_z^2}, \quad i = 1, 2, \\ \mathcal{A} &= \frac{1}{2} \left(\frac{k_{2x}}{k_{1x}} + \frac{k_{1x}}{k_{2x}} \right), \quad \text{TE}, \\ \mathcal{A} &= \frac{1}{2} \left(\frac{n_1^2 k_{2x}}{n_2^2 k_{1x}} + \frac{n_2^2 k_{1x}}{n_1^2 k_{2x}} \right), \quad \text{TM}, \end{aligned} \quad (1)$$

where TE (TM) denote the polarization of light with the electric (magnetic) field along the y axis, the coordinate system is shown in Fig. 1, and k_x is the Bloch wave number. Equation (1) defines the set of dispersion surfaces $\omega_\gamma(k_x, q_z)$, which can touch each other leading to the photonic band gap closing. This happens when the right-hand side of Eq. (1) has zero derivatives with respect to d_1, d_2 and takes the value of ± 1 . As $A > 1$, the right-hand side of Eq. (1) takes the extremum values of $\pm A$ and saddle point values ± 1 . The latter one is achieved at

$$k_{1x} d_1 = \pi m_1, \quad k_{2x} d_2 = \pi m_2, \quad (2)$$

where m_1, m_2 are positive integers. The conditions of the band degeneracy that appears at Fabri-Perot-like resonant conditions of light in each PhC layer are given by Eqs. (2), which provide the explicit position of the crossing point as

$$\begin{aligned} \frac{\omega_{m_1 m_2}^*}{c} &= \pi \sqrt{\frac{1}{n_1^2 - n_2^2} \left[\left(\frac{m_1}{d_1} \right)^2 - \left(\frac{m_2}{d_2} \right)^2 \right]}, \\ q_{z m_1 m_2}^* &= \pi \sqrt{\frac{1}{n_1^2 - n_2^2} \left[\left(\frac{m_1 n_2}{d_1} \right)^2 - \left(\frac{m_2 n_1}{d_2} \right)^2 \right]}, \\ k_x^* &= \pi [1 - (-1)^{m_1 + m_2}] / 2d, \end{aligned} \quad (3)$$

the diabolic point wavelength is $\lambda_{m_1, m_2}^* = 2\pi c / \omega_{m_1, m_2}^*$. Since the diabolic point is determined by the parameters m_1 and m_2 , in the following we denote each such point by a pair of integers (m_1, m_2) . The combination (m_1, m_2) corresponds to the crossing of $\gamma = m_1 + m_2$ and $\gamma = m_1 + m_2 + 1$ modes. As an example, Eq. (3) defines the touching point of the isofrequency curves of the modes with $\gamma = 6, 7$ shown in Fig. 5(a).

Using the transfer matrix approach [69] we obtained the ratio of the field amplitudes $\mathcal{E}_\alpha^1, \mathcal{E}_\alpha^2$ in the PhC's layers 1 and 2 for each of the two crossing modes in the diabolic point (m_1, m_2) . For one of the modes the amplitudes in both layers are the same [the case of $\gamma = 7$, red curve in Fig. 5(c)], so this mode is highly absorbed, while for the second mode [$\gamma = 6$, blue curve in Fig. 5(c)] the amplitudes are different and depend on the values of m_1, m_2 :

$$\frac{|\mathcal{E}_\alpha^1|}{|\mathcal{E}_\alpha^2|} = \begin{cases} 1, & \left(\frac{\partial \omega_\alpha}{\partial q_z} \right)_{q_{z m_1 m_2}^*, k_x^*} < \left(\frac{\partial \omega_\beta}{\partial q_z} \right)_{q_{z m_1 m_2}^*, k_x^*}, \\ \frac{d_1 m_2}{d_2 m_1} < 1, & \text{otherwise,} \end{cases} \quad (4)$$

where α, β are the serial numbers of the crossing modes, i.e., $m_1 + m_2, m_1 + m_2 + 1$. Each case can be recognized in Fig. 4(b) by the slope of the touching dispersion curves. According to Eq. (4), near each diabolic point the field amplitudes in the two adjacent layers are equal for a weakly sloping dispersion curve, while they are different for a strongly sloping curve [see Fig. 4(b); note ordinate is λ , but not ω]. As an example, the latter ones are highlighted for diabolic points $(m_1, 1)$ [Fig. 4(b)]. It stems from Eq. (4) that the maximal field difference in the neighboring layers is achieved at $(m_1, 1)$ points indicating the existence of the well localized states with extremely low losses [see blue curve in Fig. 5(c)]. Increasing of the resonance order m_1 in the first layer improves the localization and decreases the losses.

Note the position of the diabolic points [Eq. (3)] does not depend on the light polarization. For TM polarization additional points appear, which correspond to $k_{1x} d_1 + k_{2x} d_2 = m\pi$ and $\frac{n_2^2 k_{2x}}{n_1^2 k_{1x}} + \frac{n_2^2 k_{1x}}{n_1^2 k_{2x}} = 2$, i.e., at $\mathcal{A} = 1$. It gives

$$\begin{aligned} \frac{\omega_m^*}{c} &= m\pi \frac{\sqrt{n_1^2 + n_2^2}}{n_1^2 d_1 + n_2^2 d_2}, & q_{z m}^* &= \frac{\omega_m^*}{c} \frac{n_1 n_2}{\sqrt{n_1^2 + n_2^2}}, \\ k_x &= \pi [1 - (-1)^m] / 2d. \end{aligned} \quad (5)$$

These additional crossing points appear as a result the Brewster effect at the interfaces between the layers inside the PhC and do not emerge in our studies.

As the degeneracy points appear at the edges or in the center of the Brillouin zone, i.e., at $k_x = 0$ and $k_x = \pi/d$, let us consider the propagation constants of the TE-polarized modes shown in Fig. 4(b) for these k_x values by dashed and solid curves, respectively. Shaded regions are the projected bands, the white ones stand for the PBGs. Each crossing point is labeled by the two integer numbers (m_1, m_2) according to Eq. (3). As seen the waists of the maxima of the spectral-angular dependence of transmission [see Fig. 4(a)] correspond exactly to the crossing points with indexes $(m_1, m_2) = (m_1, 1)$. Since $m_2 = 1$ in all these points, the mode with single antinode of the field in low refractive index layer specifies the transmission maxima and it suffers the degeneracy as was demonstrated above for the point (5,1) at $\lambda_{5,1}^* = 808$ nm [Fig. 5(c)]. Due to the periodicity of the PhC band structure, the crossing points of the dispersion curves and the nodes in the angular-wavelength transmission spectrum appear at the same wavelengths and are distanced by the reciprocal lattice vector length h .

The interrelation of the narrowing of the transmission maxima and diabolic points can be discussed in terms of the topological effects in the PhC band structure as changing the symmetry of eigenstates at the crossing points. The considered PhC has the inversion symmetry with respect of the center of one of the layers. Let us put the origin of the coordinate system in the center of the layer with the refractive index n_2 . In this case the PhC eigenmodes $E_\gamma(x, z)$ in the center and at the edge of the Brillouin zone can be divided in symmetric or antisymmetric ones [39,70]. The amplitude of the symmetric mode $|E_\gamma(x, z)|$ has an antinode at $x = 0$, while for antisymmetric $|E_\gamma(0, z)| = 0$. For example, in Fig. 5(c) the sixth mode is symmetric, while the seventh mode is antisymmetric.

The band crossing is accompanied by the inversion of the symmetry of the eigenstates. The band inversion is illustrated by Fig. 6(a), which demonstrates the dispersion surfaces for $\gamma = 6, 7$ with the diabolic point, i.e., conical intersections of the surfaces. At this point the photonic band gap comes to zero as shown in the projected band diagram. At the edges of the Brillouin zone the eigenstates are symmetric, which is indicated by the red curves, while in the center of the zone there are symmetric (red curve) and antisymmetric states (blue curve), which cross in the diabolic point leading to topological phase transition. As a result, each dispersion sheet at $k_x = 0$ has the states of both types of symmetry. The intersection of the states with different symmetry is an intrinsic property of all crossing points of the considered photonic system. These points are symmetry protected and robust to the variation of the refractive indexes and thicknesses of the PhC layers. As seen from the explicit expression of the position of the diabolic points given by Eqs. (3) and (5), any variation of the PhC parameters results in the spectral shift of the diabolic point without opening the gap. It is worth noting that under the violation of the PhC symmetry the eigenstates lose their symmetry, the gap opens, and the crossing point disappears, which can be demonstrated by adding the third layer to the unit cell.

TABLE I. The Zak phase of 6 and 7 bands depending on q_z .

γ	q_z range	Zak phase, ϕ
6	$q_{z41}^* < q_z < q_{z51}^*$	0
	$q_{z51}^* < q_z$	π
7	$q_{z52}^* < q_z < q_{z51}^*$	π
	$q_{z51}^* < q_z < q_{z61}^*$	0

Changing the symmetry of eigenstates at the topological phase transition in the diabolic point of a periodic system possessing the inversion symmetry is known in solid state physics as quantization of the Zak phase ϕ [51]. The Zak phase is the topological invariant, which characterizes the topological property of bands of a 1D periodic system. It is a special type of the Berry phase for a 1D band over the Brillouin zone. The Berry phase Φ is the geometrical phase acquired by a system at translating it along the parameter loop [71]. Representing the loop as a set of N points (k_{xi}, q_{zi}) , $i = 1, \dots, N$, it can be defined as [72]

$$\Phi = -\arg(\langle \psi_1 | \psi_2 \rangle \langle \psi_2 | \psi_3 \rangle \cdots \langle \psi_{N-1} | \psi_N \rangle \langle \psi_N | \psi_1 \rangle), \quad (6)$$

where $|\psi_i\rangle = \sqrt{\varepsilon} A_\gamma(x)$ is the state at the i th point (k_{xi}, q_{zi}) at the loop and

$$\langle \psi_\alpha | \psi_\beta \rangle = \frac{1}{d} \int_{-d/2}^{d/2} \psi_\alpha^* \psi_\beta dx. \quad (7)$$

Due to the torus topology of the Brillouin zone the path can be closed over its edges. So the path is now a set of N points (k_{xi}, q_z) , where $k_{x1} = -\pi/a$, $k_{xN} = \pi/a$, and q_z is fixed, i.e., it goes around the Brillouin zone $[-h/2, h/2]$. In this case the acquired phase is the Zak phase defined in analogy with Eq. (6). Being defined for 1D periodic systems, the Zak phase for the inversion symmetric structures is quantized and takes the value of 0 or π by modulo 2π for each band depending on whether the symmetry of the states in the center and at the edge of the Brillouin zone are the same or not [39]. Here we used the Pancharatnam discrete formula instead of the continuous one for the calculation convenience [72,73], in which an additional factor of $\sqrt{\varepsilon}$ occurs according to Refs. [39,74,75]. The Zak phase depends on the band number γ and q_z . It suffers the π jump for the glued bands when the q_z parameter passes through the critical value defined by Eq. (3). In the case of the PhC considered here, the Zak phases for $\gamma = 6$ and $\gamma = 7$ bands depending on q_z are shown in Table I. The Zak phase is 0 (π) for $\gamma = 6(7)$ at $q_z < q_{z51}^*$ and, on the contrary, it is π (0) at $q_{z51}^* < q_z$ indicating the band inversion at the topological phase transition, which occurs at q_{z51}^* .

As was mentioned above, narrowing of the transmission maxima is related to rapid changing of the eigenmode fields in a PhC near the crossing point. We demonstrate the transformation of the fields of the eigenmodes $\gamma = 6, 7$ from even to odd states at the topological transition by spatial distributions of the electric field in the PhC's unit cell. These distributions are shown along the circular path in (k_x, q_z) plane around the

diabolic point in Fig. 6(b). The circumference path and round direction are shown by the arrow in Fig. 6(a). The angle φ is the angular position of a point on the loop. We choose the path in such a way that it has the radius of $r = h/10$ and is centered at the diabolic point shown by the minimum of the color map in Fig. 6(a). The A and S sections shown by dashed segments in Fig. 6(b) for the dispersion surface with $\gamma = 6$ correspond to field distribution at points (k_x, q_z) : $(0, q_{z51}^* + h/10)$ and $(0, q_{z51}^* - h/10)$, respectively, i.e., $\varphi = \pi/2$ and $\varphi = 3\pi/2$. On the contrary, for $\gamma = 7$ the $A(S)$ section corresponds to $\varphi = 3\pi/2$ ($\pi/2$). As seen at S section of Fig. 6(b), an even state that is highly localized in a nonabsorbing layer becomes odd at A section having similar field amplitudes in both layers. The field in the absorbing layer appears as rings near the internal and external circular edges of the figure ($x = \pm d/2$). As a result, for the light frequencies above (below) the diabolic point, the seventh (sixth) mode specifies the transmission maximum. Since the topological transition occurs in the diabolic point, the transformation of the mode with small attenuation to the one with high attenuation takes place for the arbitrary small path around it. So an arbitrarily small deviation from the Bragg angle near the diabolic point leads to crucial changes of the field forming nodes in the transmission maximum.

The topological transition is also manifested by acquiring the Berry phase along the loop of the wave vector trajectory around the degeneracy point. It appears as a π phase jump of the eigenstate at the first and the end points of the closed path [Fig. 6(b)]. Although the absolute phase of the Bloch mode is not defined, the geometric phase Φ is gauge invariant and robust against the deformation of the loop. In the considered case the gauge is chosen in such a way that $\langle \psi_i | \psi_{i+1} \rangle / |\langle \psi_i | \psi_{i+1} \rangle| = 1$, where $i = 1, \dots, N-1$, leading to $\Phi = -\arg(\langle \psi_N | \psi_1 \rangle) = \pi$. This accumulated phase remains the same while the path embraces the diabolic point and equals zero otherwise indicating topological transition in the PhC.

Another remarkable property of the light transmission through the PhC is the staggering maxima of the spectral-angular dependence of the PhC transmission. This effect can be described in the following way. Let us consider again the maximum near $(k_x, \lambda_{5,1}^*) = (0, 808 \text{ nm})$ in Fig. 4(a). It appears owing to low losses of the sixth mode for $\lambda > \lambda_{5,1}^*$ and the seventh mode for $\lambda < \lambda_{5,1}^*$. Importantly that when passing the light wavelength through the diabolic point (5,1) the field passes continuously from the sixth dispersion sheet to the seventh one. It is shown in Fig. 7(a) by changing the wavelength while keeping $k_x = 0$, i.e., along the vertical line ($k_x = 0$) in Fig. 4(a). It can be seen that the field absorption rises when moving away from the diabolic point [Fig. 7(b)]. Indeed the seventh mode becomes waveguidelike as the light wavelength decreases. Transition to the waveguide propagation corresponds to the light wavelength $\lambda_{m_1}^{\text{wg}} = \lambda_{m_1,0}^*$ in which we have to take $m_2 = 0$ formally. This wavelength does not actually correspond to the PBG degeneracy, as shown in Fig. 4(b) where the crossovers to the waveguide regime are shown by the “+” symbols. At $\lambda_{m_1}^{\text{wg}}$ the equality of $q_{zm_1}^*/(\omega_{m_1,0}^*/c) = n_2$ is exact and the electric field of the $(m_1 + 1)$ th mode has a uniform distribution in low refractive index layers with the same amplitude as in high refractive

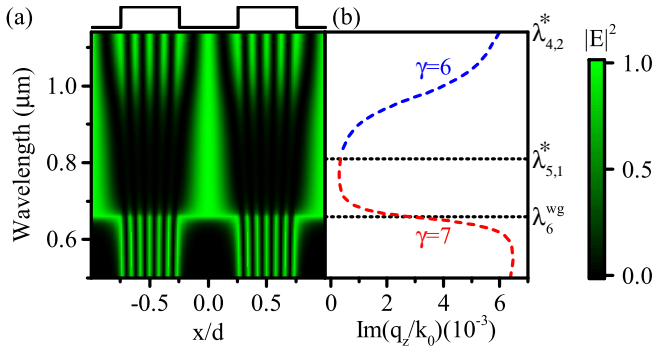


FIG. 7. (a) The spectral dependence of the electric field squared of modes $\gamma = 6$ and $\gamma = 7$ at $\lambda > \lambda_{5,1}^*$ and $\lambda < \lambda_{5,1}^*$, respectively, when $k_x = 0$. The top inset is the refractive index profile. (b) Spectral dependence of the attenuation constants of the same modes.

index layers [Fig. 7(a)]. In the considered case this transition appears at the wavelength of λ_6^{wg} .

On the other hand, as underlined above, the amplitudes of the electric field in both PhC's layers become equal ($|\mathcal{E}_6^1| = |\mathcal{E}_6^2|$) again as the wavelength increases and approaches the diabolic point (4,2) [Eq. (4)]. In both cases, moving away from the diabolic point $\lambda_{5,1}^*$ leads to the growth of the field localization in absorbing PhC layers. It leads to the appearance of the transmission spots near $(k_x, \lambda_{5,1}^*)$, where $k_x = 0, \pm h, \dots$. So each maximum corresponds to the parts of the dispersion curves, which have the propagation constant equal approximately to the smaller refractive index n_2 [$\text{Re}(q_z/k_0) \approx n_2$], pass through the diabolic point $(m_1, 1)$ connecting two dispersion sheets, and lie between the waveguide propagation starting at the point $(m_1 + 1, 0)$, and up to the point $(m_1 - 1, 2)$. These regions of dispersion curves with smallest losses are highlighted in Fig. 4(b) and appear alternatively in the center and edges of the Brillouin zone on the wavelength scale as seen in Fig. 4(b). So the maxima staggering appears.

To accomplish the description of the revealed properties of the Borrmann effect associated with diabolic points we emphasize that they are related with high refractive index contrast of the PhC. First, as explicitly seen from Eq. (3) the diabolic points shift to higher frequencies at decreasing the refractive index contrast $|n_1 - n_2|$, moving the nodal points in the spectral-angular dependence of the PhC transmission to shorter wavelengths away from visible range. Second, high refractive index contrast of PhC layers leads to exciting of several eigenmodes in the PhC with significant amplitudes when the light wave impinges on the PhC facet. As was shown, some of them experience the degeneracy forming the described features of the Borrmann effect. Reduction of the refractive index contrast of PhC layers eliminates excitation of high order modes removing pronounced properties of the Borrmann effect. Particularly, for a PhC with low refractive index contrast the single mode $\gamma = 1$ possessing homogeneous electric field distribution is excited at normal incidence. This mode does not experience the degeneracy and cannot give transmission maximum at normal incidence shown for the considered PhC possessing high refractive index contrast. So the demonstrated properties of

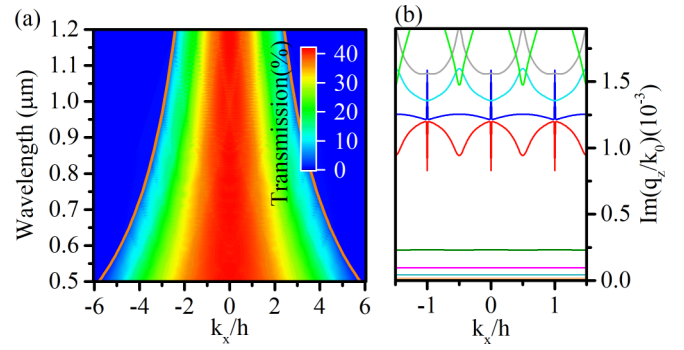


FIG. 8. (a) Calculated spectral-angular dependence of transmission of the PhC with losses in low refractive index layers, and (b) attenuation constants of the modes at $\lambda = 808$ nm for this PhC. The curve colors are the same as in Fig. 5(a).

the Borrmann effect are peculiar to the photonics in contrast to x rays.

In the last part of the article we demonstrate a crucial difference of the light transmission through the PhC with losses in low refractive index layers as compared to the PhC with absorption in high refractive index layers considered above. Let us assign the losses to the layers with n_2 : $n_1(800 \text{ nm}) = 1.76$, $n_2(800 \text{ nm}) = 1.11 + i1.6 \times 10^{-3}$ and keep the same layer thicknesses. In this case the light transmission is increased manyfold compared to the previous PhC and does not reveal multiple maxima [Fig. 8(a)]. We attribute this difference of the light transmission of both structures to the contribution of many waveguide modes localized in nonabsorbing layers. Indeed, transfer of a small imaginary part of the refractive indexes from the layer with n_1 to n_2 changes substantially the mode decay while keeping isofrequency curves of $\text{Re}(q_z)$ unchanged [Fig. 8(b)]. As can be seen, the set of waveguide modes in this case has the smallest attenuation constant, which varies by no more than 3% in the whole range of the k_x variation. So the existence of multiple waveguide modes with negligible variation of $\text{Im}(q_z)$ leads to a monotonic decrease of the light transmission at increasing the angle of incidence, which is attributed to the Fresnel reflection at the PhC edges [Fig. 8(a)].

IV. CONCLUSION

Summing up, in this work we discuss the results of our experimental and theoretical studies of spectral features of the Borrmann effect in absorbing 1D PhC in the Laue diffraction scheme. Compared to the x-ray Borrmann effect in the ordinary crystals, the fascinating properties of this effect were revealed in artificial photonic systems. We show both experimentally and theoretically the anomalous high transmission of the PhC not only at the Bragg angles of incidence, but at the normal incidence as well. It is important that in the last case the Bragg diffraction is absent for the x rays in crystals and the Borrmann effect does not appear. Moreover, a chessboardlike set of maxima in the spectral-angular dependence of PhC transmission is obtained, accompanied by angular narrowing of each maximum at certain wavelengths associated with the diabolic points. These features of the Borrmann effect are

discussed in terms of the topological transition in a PhC where the symmetry inversion of the eigenstates and discontinuous jump of the Zak phase take place. We note that the revealed features are intimately related to the high refractive index contrast and large period of the PhC, which result in the appearance of a number of diabolic points in the PhC band structure.

Finally we demonstrate by numerical calculations the qualitative difference of the light transmission through the PhCs with absorption located in the PhC layers with high or low refractive index. Namely, if the losses are inherent to the layers with low refractive index, the Borrmann effect disappears because of the waveguide modes transfer light energy through the PhC.

We would like to emphasize that as compared to previous works on topological properties of 1D PhCs considered in the the Bragg geometry of light diffraction, our studies are carried out for the Laue diffraction scheme, so that no PBGs are formed and several eigenmodes are excited simultaneously. As a result, the diabolic points in the 1D PhCs band structure have a strong effect on the transmission spectra without tuning of the PhC parameters as required at the Bragg geometry. For our structure, the existence of diabolic points is due to the symmetry of the considered PhC. Topological properties of these points were confirmed by the discontinuous Zak phase jump, carrying the Berry phase and changing the symmetry of the PhC eigenstates. An important result is the redistribution of the optical field between the adjacent PhC layers of different absorption in the vicinity of the diabolic point, resulting from the eigenstates' symmetry change. We demonstrate that this redistribution is especially strong near the topological transition, which makes the light transmission extremely sensitive to the angle of incidence for the case of a PhC with periodic distribution of light losses. In the experiment this

appears as an angular narrowing point in the PhC wavelength-angular transmission spectrum. So the usage of periodically lossy 1D PhCs that makes the system non-Hermitian allows us to study the topological properties of the PhC using the bulk instead of surface states. One more meaningful result is the strong difference of the light localization in PhC layers for the neighboring diabolic points from the single dispersion sheet [see Eq. (4)]. We demonstrate that wavelength detuning from the diabolic points labeled as $(m_1, 1)$ leads to a pronounced increase of the field amplitude in absorbing layers, which results in the wavelength boundedness of PhC transmission maxima.

These unique properties of the Laue diffraction in absorbing PhC are intrinsic to photonic systems, which allow us to achieve high contrast of the refractive index of the constituting layers. In turn this leads to the appearance of crossing points in the band structure and waveguide modes. We assert that the revealed properties of the Borrmann effect is a way for the observation of the topological phase transition owing to light losses of the PhC. This approach can be further improved in order to resolve other diabolic points by using a more complex spatial profile of the light absorption in a PhC. High sensitivity of the field distribution in a PhC to variation of the parameters of the structure near the crossing point allows us to use it for the control over the light-matter interaction.

ACKNOWLEDGMENTS

The authors are thankful to Professor B. I. Mantsyzov for fruitful and encouraging discussions. This work was partially supported by Russian Foundation for Basic Research, Grant 19-02-00826.

-
- [1] G. Borrmann, *Phys. Z* **42**, 157 (1941).
 - [2] G. Borrmann, *Z. Phys.* **127**, 297 (1950).
 - [3] H. N. Campbell, *J. Appl. Phys.* **22**, 1139 (1951).
 - [4] H. Cole, F. W. Chambers, and C. G. Wood, *J. Appl. Phys.* **32**, 1942 (1961).
 - [5] S. Lagomarsino, G. Stefani, P. Castrucci, P. Letardi, F. Scarinci, G. Savelli, and A. Tebano, *Phys. Rev. B* **45**, 6953 (1992).
 - [6] G. C. Baldwin, J. C. Solem, and V. I. Gol'danskii, *Rev. Mod. Phys.* **53**, 687 (1981).
 - [7] B. W. Batterman and H. Cole, *Rev. Mod. Phys.* **36**, 681 (1964).
 - [8] E. N. Leith, A. Kozma, J. Upatnieks, J. Marks, and N. Massey, *Appl. Opt.* **5**, 1303 (1966).
 - [9] E. J. Saccocio, *J. Appl. Phys.* **38**, 3994 (1967).
 - [10] V. V. Aristov, V. S. Shekhtman, and V. B. Timofeev, *Phys. Lett. A* **28**, 700 (1969).
 - [11] L. Carretero, R. F. Madrigal, A. Fimia, S. Blaya, and A. Beléndez, *Opt. Lett.* **26**, 786 (2001).
 - [12] V. B. Novikov and T. V. Murzina, *Opt. Lett.* **42**, 1389 (2017).
 - [13] W. J. Tomlinson and G. D. Aumiller, *Appl. Opt.* **14**, 1100 (1975).
 - [14] V. B. Novikov, S. E. Svyakhovskiy, A. I. Maydykovskiy, T. V. Murzina, and B. I. Mantsyzov, *J. Appl. Phys.* **118**, 193101 (2015).
 - [15] V. A. Bushuev, L. V. Dergacheva, and B. I. Mantsyzov, *Phys. Rev. A* **95**, 033843 (2017).
 - [16] V. A. Bushuev, B. I. Mantsyzov, and A. A. Skorynin, *Phys. Rev. A* **79**, 053811 (2009).
 - [17] S. E. Svyakhovskiy, A. A. Skorynin, V. A. Bushuev, S. V. Chekalin, V. O. Kompanets, A. I. Maydykovskiy, T. V. Murzina, V. B. Novikov, and B. I. Mantsyzov, *J. Opt. Soc. Am. B* **30**, 1261 (2013).
 - [18] V. B. Novikov, A. I. Maydykovskiy, B. I. Mantsyzov, and T. V. Murzina, *Phys. Rev. B* **93**, 235420 (2016).
 - [19] D. A. Kopylov, S. E. Svyakhovskiy, L. V. Dergacheva, V. A. Bushuev, B. I. Mantsyzov, and T. V. Murzina, *Phys. Rev. A* **93**, 053840 (2016).
 - [20] I. V. Shutov, I. A. Ozheredov, A. V. Shumitski, and A. S. Chirkin, *Opt. Spectrosc.* **105**, 79 (2008).
 - [21] C. Kulkarni, D. Di Nuzzo, E. Meijer, and S. C. Meskers, *J. Phys. Chem. B* **121**, 11520 (2017).
 - [22] K. A. Suresh, *Mol. Cryst. Liq. Cryst.* **35**, 267 (1976).
 - [23] R. Nityananda, U. Kini, S. Chandrasekhar, and K. Suresh, *Pramana* **1**, 325 (1975).

- [24] S. Aronishidze, V. Dmitrienko, D. Khoshtariya, and G. Chilaya, *JETP Lett.* **32**, 17 (1980).
- [25] S. Endo, T. Kuribara, and T. Akahane, *Jpn. J. Appl. Phys.* **22**, L499 (1983).
- [26] V. A. Belyakov, *Mol. Cryst. Liq. Cryst.* **612**, 81 (2015).
- [27] Z. Zhang and S. Satpathy, *Phys. Rev. Lett.* **65**, 2650 (1990).
- [28] W. Wang and S. A. Asher, *J. Am. Chem. Soc.* **123**, 12528 (2001).
- [29] M. V. Bogdanova, Y. E. Lozovik, and S. L. Eiderman, *J. Exp. Theor. Phys.* **110**, 604 (2010).
- [30] A. P. Vinogradov, Y. E. Lozovik, A. M. Merzlikin, A. V. Dorofeenko, I. Vitebskiy, A. Figotin, A. B. Granovsky, and A. A. Lisyansky, *Phys. Rev. B* **80**, 235106 (2009).
- [31] S. G. Erokhin, A. A. Lisyansky, A. M. Merzlikin, A. P. Vinogradov, and A. B. Granovsky, *Phys. Rev. B* **77**, 233102 (2008).
- [32] A. Cebrecos, R. Picó, V. Romero-García, A. M. Yasser, L. Maigyte, R. Herrero, M. Botey, V. J. Sánchez-Morcillo, and K. Staliunas, *Appl. Phys. Lett.* **105**, 204104 (2014).
- [33] A. B. Khanikaev, A. B. Baryshev, P. B. Lim, H. Uchida, M. Inoue, A. G. Zhdanov, A. A. Fedyanin, A. I. Maydykovskiy, and O. A. Aktsipetrov, *Phys. Rev. B* **78**, 193102 (2008).
- [34] A. Figotin and I. Vitebskiy, *Phys. Rev. B* **77**, 104421 (2008).
- [35] I. E. Razzdol'skii, T. V. Murzina, O. A. Aktsipetrov, and M. Inoue, *JETP Lett.* **87**, 395 (2008).
- [36] A. B. Khanikaev, S. H. Mousavi, W.-K. Tse, M. Kargarian, A. H. MacDonald, and G. Shvets, *Nat. Mater.* **12**, 233 (2013).
- [37] Z. Wang, Y. Chong, J. D. Joannopoulos, and M. Soljačić, *Nature (London)* **461**, 772 (2009).
- [38] X. Cheng, C. Jouvaud, X. Ni, S. H. Mousavi, A. Z. Genack, and A. B. Khanikaev, *Nat. Mater.* **15**, 542 (2016).
- [39] M. Xiao, Z. Q. Zhang, and C. T. Chan, *Phys. Rev. X* **4**, 021017 (2014).
- [40] M. Xiao, G. Ma, Z. Yang, P. Sheng, Z. Zhang, and C. T. Chan, *Nat. Phys.* **11**, 240 (2015).
- [41] K. H. Choi, C. W. Ling, K. F. Lee, Y. H. Tsang, and K. H. Fung, *Opt. Lett.* **41**, 1644 (2016).
- [42] L. Ge, L. Liu, M. Xiao, G. Du, L. Shi, D. Han, C. T. Chan, and J. Zi, *J. Opt.* **19**, 06LT02 (2017).
- [43] F. Li, X. Huang, J. Lu, J. Ma, and Z. Liu, *Nat. Phys.* **14**, 30 (2018).
- [44] C. Kane and T. Lubensky, *Nat. Phys.* **10**, 39 (2014).
- [45] F. D. M. Haldane and S. Raghu, *Phys. Rev. Lett.* **100**, 013904 (2008).
- [46] M. Hafezi, S. Mittal, J. Fan, A. Migdall, and J. Taylor, *Nat. Photon.* **7**, 1001 (2013).
- [47] M. A. Bandres, S. Wittek, G. Harari, M. Parto, J. Ren, M. Segev, D. N. Christodoulides, and M. Khajavikhan, *Science* **359**, eaar4005 (2018).
- [48] L. Lu, L. Fu, J. D. Joannopoulos, and M. Soljačić, *Nat. Photon.* **7**, 294 (2013).
- [49] J. Noh, S. Huang, D. Leykam, Y. D. Chong, K. P. Chen, and M. C. Rechtsman, *Nat. Phys.* **13**, 611 (2017).
- [50] L. Lu, Z. Wang, D. Ye, L. Ran, L. Fu, J. D. Joannopoulos, and M. Soljačić, *Science* **349**, 622 (2015).
- [51] J. Zak, *Phys. Rev. Lett.* **62**, 2747 (1989).
- [52] W. S. Gao, M. Xiao, C. T. Chan, and W. Y. Tam, *Opt. Lett.* **40**, 5259 (2015).
- [53] W. Gao, M. Xiao, B. Chen, E. Y. B. Pun, C. T. Chan, and W. Y. Tam, *Opt. Lett.* **42**, 1500 (2017).
- [54] C. Qian, K. H. Choi, R. P. H. Wu, Y. Zhang, K. Guo, and K. H. Fung, *Opt. Express* **26**, 5083 (2018).
- [55] Y. Ota, R. Katsumi, K. Watanabe, S. Iwamoto, and Y. Arakawa, *Commun. Phys.* **1**, 86 (2018).
- [56] Q. Wang, M. Xiao, H. Liu, S. Zhu, and C. T. Chan, *Phys. Rev. X* **7**, 031032 (2017).
- [57] Z. Liu, Q. Zhang, F. Qin, D. Zhang, X. Liu, and J. J. Xiao, *Phys. Rev. B* **99**, 085441 (2019).
- [58] J. M. Zeuner, M. C. Rechtsman, Y. Plotnik, Y. Lumer, S. Nolte, M. S. Rudner, M. Segev, and A. Szameit, *Phys. Rev. Lett.* **115**, 040402 (2015).
- [59] O. N. Kirillov, A. A. Mailybaev, and A. P. Seyranian, *J. Phys. A* **38**, 5531 (2005).
- [60] C. Dembowski, H.-D. Gräf, H. L. Harney, A. Heine, W. D. Heiss, H. Rehfeld, and A. Richter, *Phys. Rev. Lett.* **86**, 787 (2001).
- [61] J. Doppler, A. A. Mailybaev, J. Böhm, U. Kuhl, A. Girschik, F. Libisch, T. J. Milburn, P. Rabl, N. Moiseyev, and S. Rotter, *Nature (London)* **537**, 76 (2016).
- [62] H. Zhou, C. Peng, Y. Yoon, C. W. Hsu, K. A. Nelson, L. Fu, J. D. Joannopoulos, M. Soljačić, and B. Zhen, *Science* **359**, 1009 (2018).
- [63] B. Zhen, C. W. Hsu, Y. Igarashi, L. Lu, I. Kaminer, A. Pick, S.-L. Chua, J. D. Joannopoulos, and M. Soljačić, *Nature (London)* **525**, 354 (2015).
- [64] V. V. Konotop and B. I. Mantsyzov, *Opt. Express* **24**, 26146 (2016).
- [65] D. M. Tsvetkov, V. A. Bushuev, and B. I. Mantsyzov, *Phys. Rev. A* **99**, 023846 (2019).
- [66] Z. Lin, H. Ramezani, T. Eichelkraut, T. Kottos, H. Cao, and D. N. Christodoulides, *Phys. Rev. Lett.* **106**, 213901 (2011).
- [67] S. E. Svyakhovskiy, A. I. Maydykovskiy, and T. V. Murzina, *J. Appl. Phys.* **112**, 013106 (2012).
- [68] M. G. Moharam, E. B. Grann, D. A. Pommet, and T. K. Gaylord, *J. Opt. Soc. Am. A* **12**, 1068 (1995).
- [69] A. Yariv and P. Yeh, *Optical Waves in Crystals* (Wiley, New York, 1984), Vol. 5.
- [70] R. L. Liboff, *Introductory Quantum Mechanics* (Pearson Education, India, 2003).
- [71] M. V. Berry and M. Wilkinson, *Proc. R. Soc. London Ser. A* **392**, 15 (1984).
- [72] R. Resta, *J. Phys.: Condens. Matter* **12**, R107 (2000).
- [73] J. K. Asbóth, L. Oroszlány, and A. Pályi, *Lect. Notes Phys.* **919**, 23 (2016).
- [74] K. Sakoda, *Optical Properties of Photonic Crystals* (Springer Science & Business Media, New York, 2004), Vol. 80.
- [75] A. Raman and S. Fan, *Phys. Rev. Lett.* **104**, 087401 (2010).